materials

MDPI

Article

Effects of Laser Power Level on Microstructural Properties and Phase Composition of Laser-Clad Fluorapatite/Zirconia Composite Coatings on Ti6Al4V Substrates

Chi-Sheng Chien [1,2], Cheng-Wei Liu [3] and Tsung-Yuan Kuo [3,*]

1 Department of Orthopaedics, Chimei Foundation Hospital, Tainan 710, Taiwan; jannie.gissing@msa.hinet.net
2 Department of Electrical Engineering, Southern Taiwan University of Science and Technology, Tainan 710, Taiwan
3 Department of Mechanical Engineering, Southern Taiwan University of Science and Technology, Tainan 710, Taiwan; ma010115@stust.edu.tw
* Correspondence: tykuo@mail.stust.edu.tw; Tel.: +886-6-2533131 (ext. 3000)

Academic Editor: Jonathan Phillips
Received: 28 February 2016; Accepted: 11 May 2016; Published: 17 May 2016

Abstract: Hydroxyapatite (HA) is one of the most commonly used materials for the coating of bioceramic titanium (Ti) alloys. However, HA has poor mechanical properties and a low bonding strength. Accordingly, the present study replaces HA with a composite coating material consisting of fluorapatite (FA) and 20 wt % yttria (3 mol %) stabilized zirconia (ZrO_2, 3Y-TZP). The FA/ZrO_2 coatings are deposited on Ti6Al4V substrates using a Nd:YAG laser cladding system with laser powers and travel speeds of 400 W/200 mm/min, 800 W/400 mm/min, and 1200 W/600 mm/min, respectively. The experimental results show that a significant inter-diffusion of the alloying elements occurs between the coating layer (CL) and the transition layer (TL). Consequently, a strong metallurgical bond is formed between them. During the cladding process, the ZrO_2 is completely decomposed, while the FA is partially decomposed. As a result, the CLs of all the specimens consist mainly of FA, $Ca_4(PO_4)_2O$ (TTCP), CaF_2, $CaZrO_3$, $CaTiO_3$ and monoclinic phase ZrO_2 (m-ZrO_2), together with a small amount of θ-Al_2O_3. As the laser power is increased, CaO, $CaCO_3$ and trace amounts of tetragonal phase ZrO_2 (t-ZrO_2) also appear. As the laser power increases from 400 to 800 W, the CL hardness also increases as a result of microstructural refinement and densification. However, at the highest laser power of 1200 W, the CL hardness reduces significantly due to the formation of large amounts of relatively soft CaO and $CaCO_3$ phase.

Keywords: fluorapatite; zirconia; laser cladding; laser power; composite coating

1. Introduction

Biomedical implants typically comprise a thin bioceramic coating deposited on a titanium (Ti) alloy substrate [1–3]. Of the various coating materials available, hydroxyapatite ($Ca_{10}(PO_4)_6(OH)_2$; HA) is one of the most commonly used since it has the same chemical composition and crystallographic structure as the apatite of living bones, and hence promotes early bonding between the implant and surrounding tissue [4–7]. HA coatings are generally deposited using a plasma spraying technique due to its short operation time, high accumulation rate, low processing cost, and low heat input. However, HA is intrinsically brittle, and hence the as-sprayed HA coatings generally have poor adhesion with the Ti substrate [8]. Moreover, under high temperature plasma spraying, the HA decomposes into impurities and low-crystallinity phases (e.g., tricalcium phosphate ($Ca_3(PO_4)_2$), tetracalcium phosphate ($Ca_4(PO_4)_2O$), and calcium oxide (CaO)). These phases cause the coating to

delaminate or flake, and can therefore lead to various medical disorders [9]. Furthermore, the HA coating and Ti substrate have very different thermal expansion coefficients. Consequently, significant residual stress is formed at the interface between the coating and the substrate during the spraying process [9]. This residual stress prompts premature coating degradation and can lead to implant failure after long-term imbedding in the human body. As a result, the need for alternative coating materials with improved structural stability under high temperature conditions has emerged as a pressing concern in recent decades.

Fluorapatite ($Ca_{10}(PO_4)_6(F)_2$; FA) has a similar level of biological activity and biocompatibility in the human body as HA. However, FA has better thermal and chemical stability, and therefore reduces the risk of pyrolysis [10–13]. Furthermore, FA has a slow bio-resorption rate, and thus promotes bone fixing and bone ingrowth [14,15]. As a result, FA has attracted significant interest as a possible substitute for HA in biomedical implant applications [16–18]. Many studies have shown that the mechanical properties and biological performance of biomedical coating materials can be enhanced through the addition of secondary phases such as zirconia (ZrO_2) or alumina (Al_2O_3) [19–26]. Among these phases, ZrO_2 is a particularly attractive choice due to its relatively high mechanical strength and fracture toughness [23–26].

The excellent mechanical, electrical, thermal and optical properties of zirconia ceramics render them useful for many structural and functional applications [27–30]. In the biomedical field, yttria-stabilized tetragonal zirconia (Y-TZP) is widely used for dental restoration work due to its high biological safety and good hydrothermal stability [31]. Various studies have shown that 3 mol % yttria (3Y-TZP) provides an ideal stabilizing effect for zirconia [27,32]. However, even though FA is known to be more thermally and chemically stable than HA, the literature contains little information regarding the mechanical and biological properties of FA coatings mixed with ZrO_2 [4,23,24,31]. Moreover, of those studies which have been performed, the coatings are generally prepared using sintering or plasma spraying techniques. In contrast to such methods, laser beams have high coherence and directionality, and thus have the potential to generate strong metallurgical bonds between the bioceramic coating layer and the substrate [33–37]. Consequently, the present study investigates the microstructural properties and phase composition of composite FA coatings containing 20 wt % yttria (3 mol %) stabilized zirconia (ZrO_2, 3Y-TZP) deposited on Ti6Al4V substrates using a laser-cladding technique. As in previous studies by the present group [38–40], the laser cladding process is performed using an Nd:YAG laser system.

In laser cladding processes, the microstructural properties and phase composition of the coatings are significantly affected by three experimental parameters, namely the specific energy ($Es = P/(V \times D)$, P: power; V: travel speed; D: laser beam diameter), the laser power density ($LPD = P/(\pi D^2/4)$) and the interaction time ($t = D/V$)). In the present study, the cladding process is performed using three different settings of the laser power and travel speed, namely 400 W/200 mm/min, 800 W/400 mm/min, and 1200 W/600 mm/min, respectively. In other words, the laser-power/travel-speed (P/V) ratio is equal to 2:1 in all of the cladding trials. Moreover, the laser spot diameter is equal to 3 mm (approximately) in every case. Consequently, the specific energy is a constant in the present study. By contrast, the laser power density increases as the laser power is increased from 400 W to 1200 W. Finally, the interaction time reduces as the travel speed increases.

2. Experiments

The cladding trials were performed using Ti6Al4V alloy plates with dimensions of 100 mm × 60 mm × 3.8 mm and the chemical composition shown in Table 1. The FA was prepared using $Ca_3(PO_4)_2$ (β-TCP, β-tricalcium phosphate) and CaF_2 (Sigma-Aldrich, St. Louis, MO, USA) powders in accordance with the solid state reaction $3Ca_3(PO_4)_2 + CaF_2 \rightarrow Ca_{10}(PO_4)_6F_2$ [41]. Briefly, the powders were mixed in a stoichiometric molar ratio of 3:1 and milled with ZrO_2 balls in ethanol for 48 h. After drying, the powder was compacted and heated at 1000 °C for 3 h in air to form solid FA cylinders. The cylinders were then ground into powder and reinforced with 20 wt % commercial ZrO_2

powder (3 mol % Y_2O_3, EE-TEC Inc., Zhongli, Taiwan). Prior to the reinforcement process, the atomic structures of the FA (JCPDS 15-0876) and ZrO_2 (3Y-TZP, JCPDS 49-1642) powders were examined using XRD (Figure 1). No separate yttria peak was detected (*i.e.*, the XRD patterns of ZrO_2 (3Y-TZP) and TZP (tetragonal ZrO_2, t-ZrO_2) are very similar). The FA/ZrO_2 powder was mixed with a polyvinyl alcohol binder ($(C_2H_4O)_n$) in a 3:1 ratio (wt %) and stirred until a slurry-like consistency was obtained. As shown in Figure 2, the Ti6Al4V substrates used in the present study were milled with two slots (each with a size of 52 mm × 44 mm × 0.8 mm). The FA/ZrO_2 + binder slurry was placed in each slot and the excess quantity removed using a stainless steel scraper. The substrate was then dried in an oven at 100 °C for 30 min under atmospheric conditions. Finally, the specimens were laser clad using an Nd:YAG laser system (ROFIN CW025, 2500 W; Rofin Sinar Technologies Inc., Hamburg, Germany) operating in a continuous-wave mode. For each specimen, the cladding process was limited to a single laser line scan.

Table 1. Chemical composition (wt %) of Ti6Al4V substrates.

Al	V	O	Fe	C	N	H	Ti
6.1	4.24	0.152	0.16	0.017	0.008	0.0006	Balance

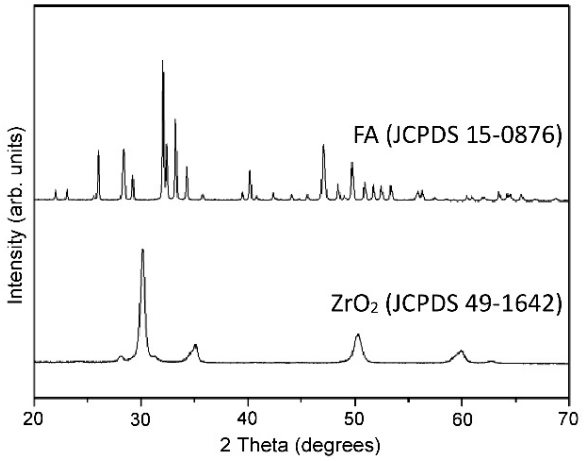

Figure 1. XRD patterns of coating powders: FA and ZrO_2 (3 mol % yttria (3Y-TZP), partially stabilized with 3 mol % Y_2O_3).

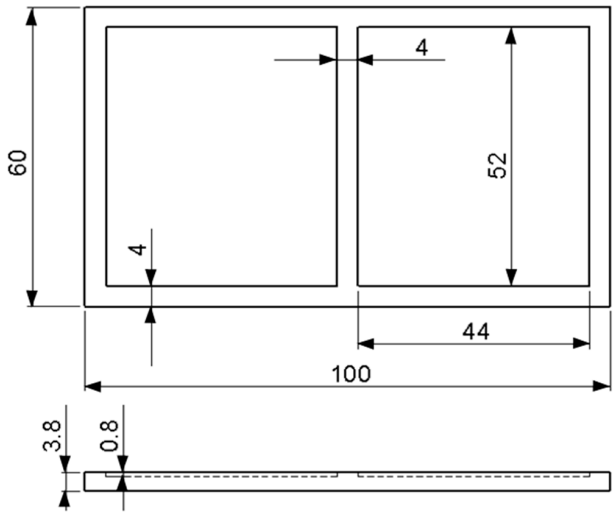

Figure 2. Schematic illustration of Ti6Al4V substrate (unit: mm).

As stated above, the cladding trials were performed using laser powers (P) and travel speeds (V) of 400 W/200 mm/min, 800 W/400 mm/min, and 1200 W/600 mm/min. The laser spot diameter was equal to approximately 3 mm in every case. Consequently, the specific energy ($Es = P/(D \times V)$) for each coating was equal to 40 J/mm^2. Furthermore, the laser power densities ($LPD = P/(\pi D^2/4)$) for the three cases were 5.66, 11.32 and 16.98 kW/cm^2, respectively. Finally, the interaction times ($t = D/V$) were 0.9, 0.45 and 0.3 s, respectively. The laser beam was guided to the workstation by an optical fiber with a core diameter of 600 μm and a focal length of 120 mm. The cladding process was performed in an Ar-shielded atmosphere (Ar flow rate: 25 L/min) with a 5° laser incident angle and a 15 mm positive defocus length. The experimental setup is shown in Figure 3.

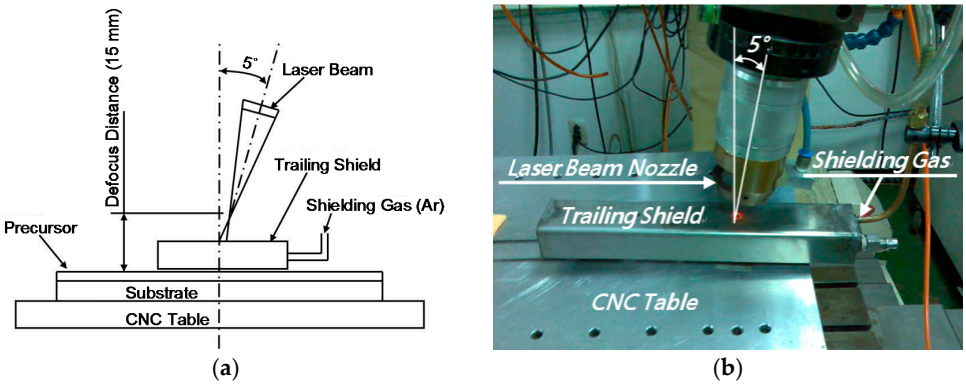

Figure 3. (**a**) Schematic illustration of Nd-YAG laser cladding system which was controlled by the computer numerical control (CNC); and (**b**) photograph of experimental setup.

The microstructures of the clad specimens were observed using SEM (JEOL JSM-6390LV, JEOL Ltd., Tokyo, Japan). In addition, the phase compositions were examined using SEM and EDS. Moreover, the various phases were identified using XRD (Cu Kα radiation, Rigaku D/Max III.V, Rigaku Ltd., Tokyo, Japan) with a 2θ scanning range of 20°~70° and a scanning rate of 2° min^{-1}. Finally, the hardness of the coatings was determined using a micro-Vickers hardness tester under a maximum indentation load of 300 g.

3. Results and Discussion

3.1. Morphology and Microstructure of Weld Beads

Figure 4 presents cross-sectional optical microscope (OM) images of the coating layers (CLs) and transition layers (TLs) of the three laser-clad specimens. As shown, for a constant Es, the depth, width and depth/width ratio (*i.e.*, aspect ratio) of the TL all increase with an increasing laser power (see also Table 2). In addition, cracks are evident within the TLs of the specimens prepared at higher laser powers of 800 W and 1200 W, respectively. The severity of the cracks increases with increasing power.

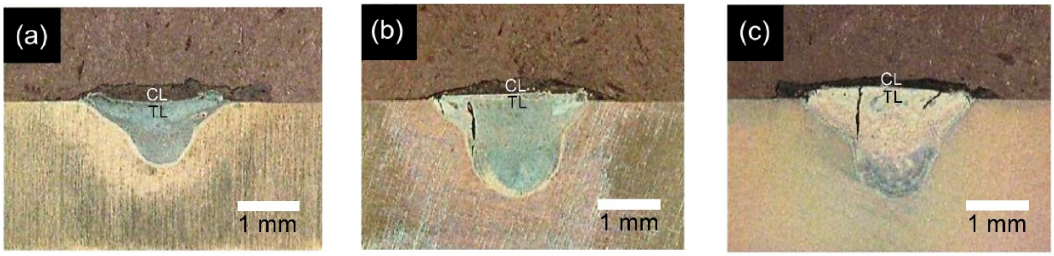

Figure 4. Optical microscope images of weld beads in fluorapatite (FA)/ZrO_2 laser-clad specimens: (**a**) 400 W, 200 mm/min; (**b**) 800 W, 400 mm/min; and (**c**) 1200 W, 600 mm/min. (Note: CL denotes coating layer and TL denotes transition layer).

Table 2. Depth-to-width ratio of TL in FA/ZrO_2 specimens prepared using different laser powers.

Sample	400 W/200 mm/min	800 W/400 mm/min	1200 W/600 mm/min
Depth (mm)	1.1	1.8	2.0
Width (mm)	2.5	2.9	3.1
Depth/Width Ratio	0.44	0.62	0.65

Given the same laser spot size and thermal diffusivity of the substrate, the size and shape of the weld fusion zone (*i.e.*, weld bead) formed in the laser cladding process depends on the laser power density (LPD). For a low LPD, the weld fusion zone tends to be shallow and bowl-shaped. By contrast, for higher LPDs, the fusion zone is deeper and has a higher aspect ratio [42]. In the present study, even though the LPD increases with an increasing laser power, the specific energy, Es, is fixed. Thus, it seems reasonable to assume that the weld fusion zone should have a similar profile for all three specimens. However, in maintaining a constant Es, the laser travel speed is increased proportionally with increasing laser power. In practice, the laser speed also affects the shape of the weld bead. Thus, as shown in Figure 3, the weld bead profile changes with a changing LPD despite the constant Es in every case.

Previous studies have shown that if the laser cladding parameters are not properly controlled, cracks are readily formed in the coating as a result of the thermal expansion mismatch between the coating and the substrate and relatively low toughness of the coating material [43]. As shown in Figure 4, cracks were not formed in any of the CLs. However, for the specimens prepared using laser powers of 800 W and 1200 W (*i.e.*, a higher travel speed, heating rate and cooling rate), cracking occurred in the TL (see Figure 4b,c). The formation of these cracks is closely related to the residual stress generated during the cladding process [44]. Moreover, the stress increases with an increasing heating and cooling rate. The OM images in Figure 4b,c show that the cracks in the two specimens initiate within the TL, *i.e.*, they do not spread from the CL. It is therefore concluded that the thermal expansion mismatch between the CL and the TL plays no role in prompting crack formation in the TL. In other words, crack initiation is dominated by the thermal stress generated by the rapid cooling rate of the substrate. More specifically, for a higher laser power (a higher laser travel speed), the cooling rate is increased. Consequently, the thermal shock within the TL is enhanced, and hence the crack severity increases. Furthermore, under a higher power level, the weld zone size also increases. As a result, a larger shrinkage stress is induced, and thus crack formation is further enhanced. Notably, however, the OM images in Figure 4 show that crack formation can be controlled through an appropriate setting of the laser power and travel speed parameters.

Figure 5 shows the surface microstructures of the CLs in the three laser-clad samples. It is seen that for all three samples, the coating has a fibrous-like morphology. Moreover, as the laser power increases, an increasing number of granular compounds are formed between the fibrous-like structures. The SEM images confirm the absence of microcracks in the CL. The lack of cracks is reasonable since the coefficients of thermal expansion (CTE) of FA and ZrO_2 (3Y-TZP) (*i.e.*, 9.1×10^{-6} K^{-1} [45] and $10\sim12 \times 10^{-6}$ K^{-1} [46], respectively) are quite close to that of the Ti6Al4V substrate (8.8×10^{-6} K^{-1} [47]) in comparison to commonly used bioceramic coatings in the past, HA (15×10^{-6} K^{-1} [47]). Hence, only limited differential expansion between the CL and the TL occurs. The addition of ZrO_2 particles with good mechanical strength and high fracture toughness further enhances the cohesive strength of the CL and suppresses microcrack formation. Therefore, the FA/ZrO_2-substrate CTE mismatch is less than that for a HA/ZrO_2-substrate system. Consequently, it can be inferred that the present FA/ZrO_2 coatings have a better adhesive strength with the Ti6Al4V substrate than HA/ZrO_2 coatings [8,29].

Figure 6 shows the interfacial microstructures of the CL and TL in the three specimens. The EDS analysis results (presented in Section 3.2) show that a significant diffusion of alloying elements occurs between the CL and TL. As a result, a strong metallurgical bond is formed between them [34]. The bonding strength of such an interface is greater than the mechanical bonding strength formed in general coating processes such as plasma spraying, sol-gel, and so on. Figure 7 presents SEM cross-sectional metallographs of the mid-section region of the CL in the various samples.

Compared with the CL surface microstructures shown in Figure 5, the quantity of fibrous structures is reduced. However, a large number of spherical and irregularly-shaped particles are observed. For the sample prepared using a low laser power (400 W), the microstructure contains many flower-like structures. However, as the power increases, the flower-like structures are replaced with spherical-like particles. In general, the SEM images presented in Figures 6 and 7 show that the higher cooling rate associated with an increased laser power results in significant microstructural refinement and densification of the CL.

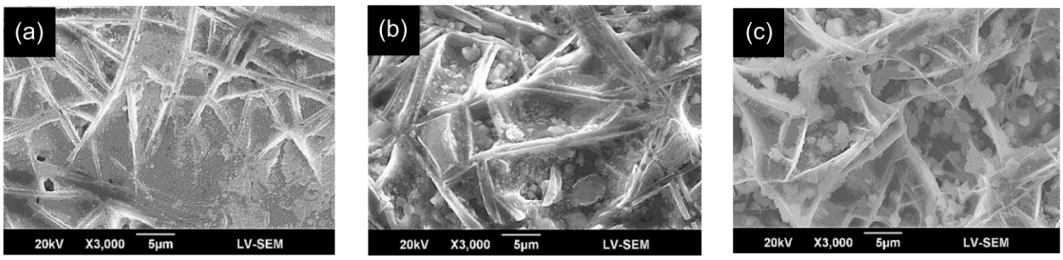

Figure 5. SEM metallographs of CL surface in FA/ZrO_2 laser-clad specimens: (**a**) 400 W, 200 mm/min; (**b**) 800 W, 400 mm/min; and (**c**) 1200 W, 600 mm/min.

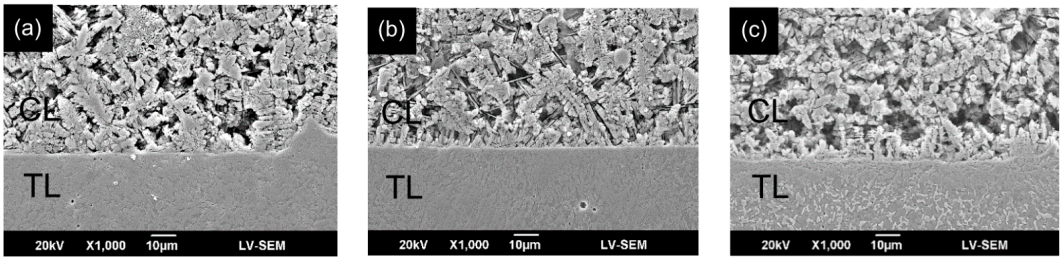

Figure 6. SEM metallographs of CL/TL interface in FA/ZrO_2 laser-clad specimens: (**a**) 400 W, 200 mm/min; (**b**) 800 W, 400 mm/min; and (**c**) 1200 W, 600 mm/min.

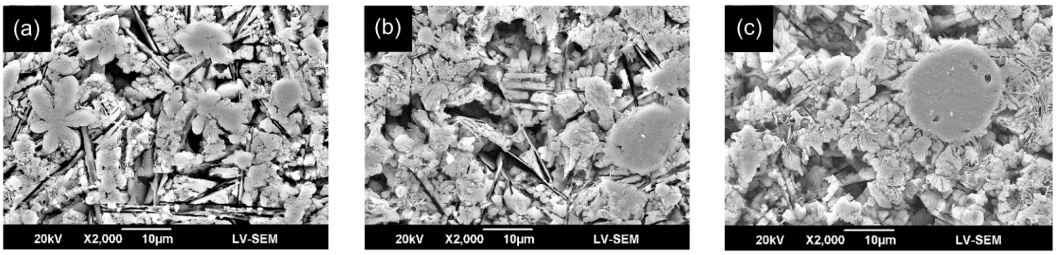

Figure 7. SEM metallographs of mid-section region of cross sectional CL in FA/ZrO_2 laser-clad specimens: (**a**) 400 W, 200 mm/min; (**b**) 800 W, 400 mm/min; and (**c**) 1200 W, 600 mm/min.

3.2. Chemical Composition Analysis of Laser-Clad Coatings

Figure 8a presents an SEM image of the CL in the sample prepared using a laser power of 1200 W. Figure 8b,c shows the EDS analysis results for globular particles A and B in Figure 8a, respectively. As shown in Figure 8b, particle A consists mainly of Ti and P. The presence of TiP compounds (Ti phosphides) [48] suggests a partial thermal decomposition of the FA content in the CL during the high-temperature cladding process, accompanied by thermal-induced melting and diffusion of Ti from the substrate. As the laser power increases, the extent of FA decomposition and Ti melting/diffusion also increases, and hence Ti phosphides of a greater size are formed, as shown in Figure 7b,c. It is noted that the present results are consistent with those of Ye *et al.* [48], who showed that a large number of Ti phosphides (Ti_xP_y) were formed when sintering Ti/FA (1:1) composite powders under temperatures of 1100 °C or 1200 °C. In general, Ti phosphides can have a wide range of compositions, and it is thus difficult to reliably determine the exact composition of Ti_xP_y by XRD analysis alone [49]. Notably, the

EDS results presented in Figure 8c, corresponding to particle B in Figure 8a, show that even under the maximum laser power of 1200 W, the CL matrix still contains a large amount of fluoride. In other words, the potential for FA residue or conversion to fluoride still exists even under high cladding temperatures, as discussed later in Section 3.3.

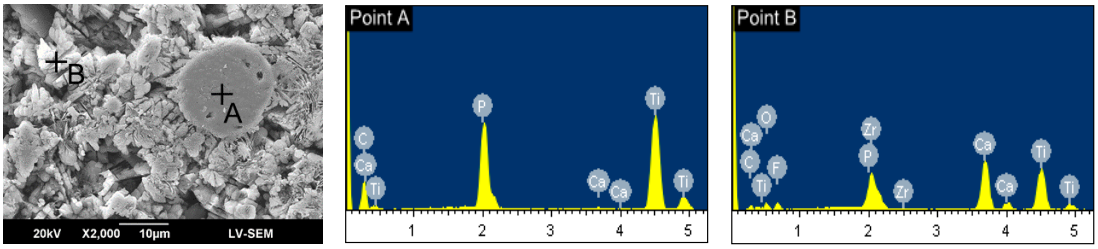

Figure 8. (**a**) SEM metallograph showing microstructure of CL in FA/ZrO_2 specimen prepared using P = 1200 W and V = 600 mm/min; (**b**) EDS analysis results for particle A in (**a**); and (**c**) EDS analysis results for particle B in (**a**).

Figure 9 presents the EDS line scanning results for the individual alloying elements of the FA/ZrO_2 cladding layer near the CL/TL interface in the specimen prepared using a laser power of 1200 W. It is seen that the Ca and F elements, *i.e.*, the main decomposition components of FA, are confined almost entirely to the CL. Previous studies have shown that in the thermal decomposition of FA, F is either vaporized as HF gas or forms fluoride [24]. Thus, the F content in the CL layer most probably comes from the FA or fluoride, but requires further XRD analysis for confirmation (see Section 3.3). The P and O ions in the coating material have the ability to diffuse rapidly from the CL to the TL due to their small radii and low activation energy. Nonetheless, as shown in Figure 9, some ions still remain within the CL. It is noted, however, that some of the P ions produced in the FA decomposition process simply vaporize in the high-temperature cladding process [37–40]. Observing the results presented in Figure 9, it is seen that the distributions of Zr in the CL and TL, respectively, are roughly the same. In other words, given an addition of 20 wt % ZrO_2 to the FA cladding material, a certain amount of Zr remains within the CL despite the high temperature diffusion effect. Furthermore, the TL retains a very high Ti content; with only a small amount of Ti diffusing to the CL. Overall, the EDS results reveal that while significant diffusion of the alloying elements occurs between the TL and the CL, the alloying elements in the TL are basically similar to the composition of the substrate, while those in the CL are similar to that of the coating material.

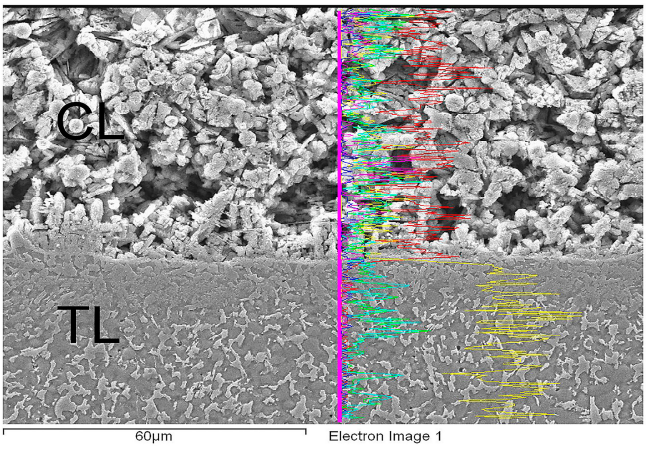

Figure 9. *Cont.*

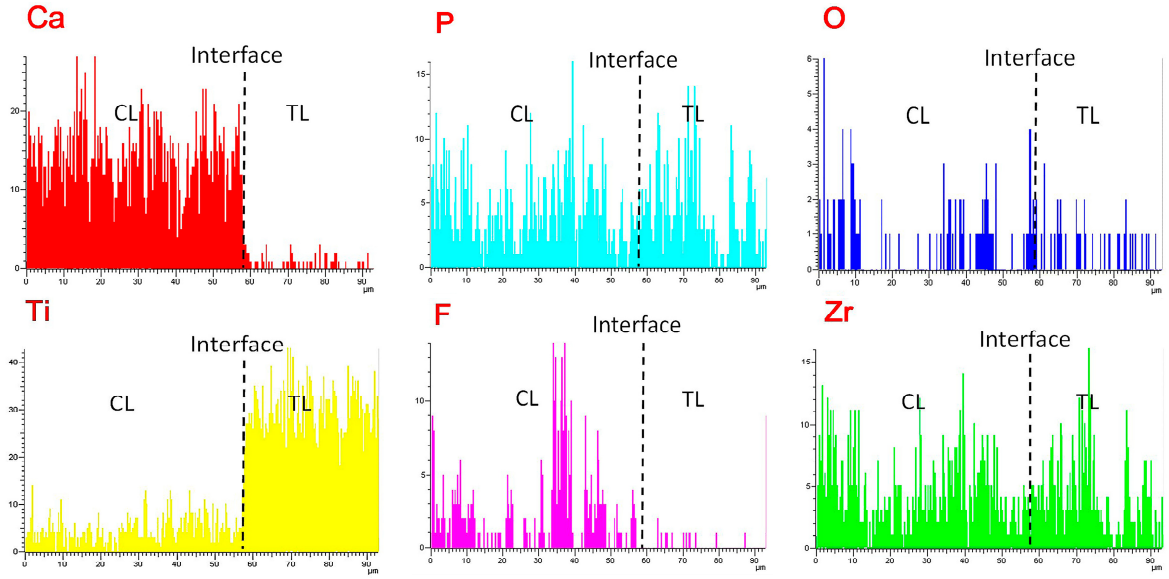

Figure 9. EDS line scan results for Ca, P, O, Ti, F and Zr contents of CL and TL in FA/ZrO_2 specimen prepared using P = 1200 W and V = 600 mm/min.

3.3. XRD Patterns of CL Surface

Figure 10 shows the XRD patterns of the CL surfaces in the three specimens. For the 400 W sample, the CL consists mainly of FA, TTCP (tetracalcium phosphate, $Ca_4(PO_4)_2O$ (JCPDS 25-1137), CaF_2 (JCPDS 35-0816), $CaZrO_3$ (JCPDS 35-0790), $CaTiO_3$ (JCPDS 22-0153), m-ZrO_2 (monoclinic phase ZrO_2, JCPDS 88-2390) and a small amount of θ-Al_2O_3 (JCPDS 23-1009). For the 800 W specimen, the CL additionally contains CaO (JCPDS 37-1497), $CaCO_3$ (JCPDS 47-1743) and a trace amount of t-ZrO_2 (tetragonal phase ZrO_2, JCPDS 80-0965). For the 1200 W specimen, the CL contains large quantities of CaO, $CaCO_3$ and TTCP, but a lesser amount of $CaTiO_3$. Furthermore, the quantity of t-ZrO_2 increases, while that of m-ZrO_2 and $CaZrO_3$ decreases. Notably, the XRD pattern also indicates the presence of trace amounts of several unknown compounds in the CL. In general, the XRD results indicate a greater tendency toward compound phase formation in the CL as the laser power is increased.

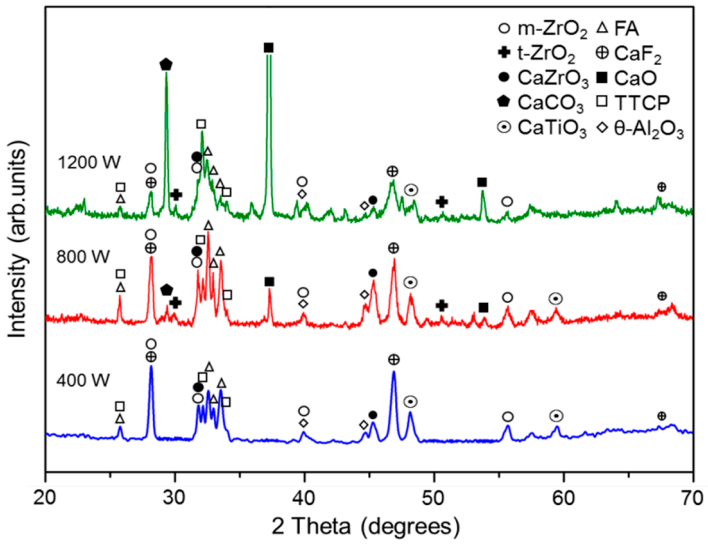

Figure 10. XRD analysis results for CLs of FA/ZrO_2 specimens prepared using different laser powers.

The FA powder used in the present study was prepared via a solid state reaction of $Ca_3(PO_4)_2$ (TCP) and CaF_2 at 1000 °C for 3 h. However, in the cladding process, the FA reverts to $Ca_3(PO_4)_2$ and

CaF_2 in accordance with Reaction (1) if the temperature remains sufficiently high for a sufficiently long period of time [23,31]. For example, Nasiri-Tabrizi and Fahami [23] reported that a partial decomposition of FA to $Ca_3(PO_4)_2$ and CaF_2 occurs at 900 °C for 1 h in the presence of zirconia. However, at higher temperatures (*i.e.*, greater than 1100 °C), CaF_2 transforms to CaO through hydrolysis, as shown in Reaction (2) [50]. Thus, the high CaO content in the CL of the present specimen prepared using a high laser power of 1200 W is most likely the result of the thermally-induced hydrolysis of CaF_2.

$$Ca_{10}(PO_4)_6F_2 \rightarrow 3Ca_3(PO_4)_2(TCP) + CaF_2 \quad (1)$$

$$CaF_2 + H_2O_{(g)} \rightarrow CaO + 2HF_{(g)} \quad (2)$$

In high temperature processes, the decomposition of FA powder without oxide addition can be described by Reaction (3). (Note that Reaction (3) is equivalent to Reaction (1) + Reaction (2)). In other words, in high temperature processes, FA decomposes as TCP and CaO [24,50]. In the present study, ZrO_2 is also added to the coating. The additional reactions which therefore take place under high density laser power irradiation are described by Reaction (4) below.

$$Ca_{10}(PO_4)_6F_{2(s)} + H_2O_{(g)} \rightarrow 3Ca_3(PO_4)_{2(s)}(TCP) + CaO_{(s)} + 2HF_{(g)} \quad (3)$$

$$Ca_3(PO_4)_{2(s)}(TCP) + 2CaO_{(s)} + ZrO_{2(s)} \rightarrow Ca_4(PO_4)_2O(TTCP) + CaZrO_3 \quad (4)$$

Ben and Bouaziz [24] examined the decomposition of FA doped with ZrO_2, and showed that given sufficient time and temperature, the decomposed TCP and CaO react with the ZrO_2 to produce TTCP and $CaZrO_3$. In addition, many researchers have analyzed the reaction between ZrO_2 and CaO in accordance with Reaction (5) [4,24,29,51].

$$CaO_{(S)} + ZrO_{2(S)} \rightarrow CaZrO_{3(S)} \quad (5)$$

In the XRD patterns in Figure 10, a peak corresponding to the original ZrO_2 powder (3Y-TZP, XRD pattern similar to t-ZrO_2) is absent for the 400 W specimen. Moreover, only small quantities of ZrO_2 are detected in the 800 W and 1200 W samples. In other words, most of the ZrO_2 particles melt and undergo phase transformation during the laser cladding process. However, FA is still present in all three samples. Thus, it is inferred that even though the original FA powder melts completely during the laser-cladding process, the high thermal stability of the FA powder and the short residence time of the powder at high temperature result in only a partial decomposition of the FA to TTCP and CaO. However, as the laser power increases, the extent of FA decomposition also increases. Thus, for the specimens prepared using higher laser powers of 800 W and 1200 W, respectively, the intensity of the TTCP and CaO peaks in the XRD patterns increases.

Under the high temperatures produced during the laser cladding process, the ZrO_2 particles reside in a molten state and the diffusion of Ca ions into the ZrO_2 particles is enhanced. Consequently, $CaZrO_3$ is formed during cooling in accordance with Reaction (5) above. Furthermore, CaO is unstable and reacts with CO_2 to form calcium carbonate ($CaCO_3$) in air [31]. As the temperature increases, more of the original FA powder decomposes as CaO, and hence the quantity of $CaCO_3$ increases. In addition, Al_2O_3 is produced via the reaction between Al atoms diffused from the substrate and the coating material atoms or environmental O atoms. Finally, $CaTiO_3$ is produced through a reaction between the decomposed or melted FA and the Ti6Al4V substrate.

For the 400 W sample, the XRD pattern indicates the presence of both m-ZrO_2 and $CaZrO_3$ compounds. For the sample prepared with a higher power of 800 W, the intensity of the m-ZrO_2 and $CaZrO_3$ peaks increases and a trace amount of t-ZrO_2 emerges. However, for the sample prepared using the highest power of 1200 W, the intensity of the t-ZrO_2 peak increases, but that of the m-ZrO_2 and $CaZrO_3$ peaks decreases. In other words, the original ZrO_2 (3Y-TZP) powder melts more completely under high-energy laser irradiation. During the cooling and solidification phase, an allotropic transformation of the ZrO_2 compound takes place from the cubic phase (c-ZrO_2 2370–2680 °C (melting point)) to the tetragonal phase (t-ZrO_2, 1170 °C–2370 °C), and finally to the

monoclinic phase (m-ZrO_2, room temperature–1170 °C) [32]. For laser cladding at 400 W, the t-ZrO_2 phase has sufficient time to transform to m-ZrO_2 due to the lower cooling rate (*i.e.*, the lower travel speed). As a result, the ZrO_2 exists almost entirely in the monoclinic phase. However, for higher laser powers of 800 W and 1200 W, respectively, insufficient time exists for t-ZrO_2 transformationto m-ZrO_2 and consequently the quantity of t-ZrO_2 increases while that of m-ZrO_2 decreases. Notably, no c-ZrO_2 is observed in any of the XRD patterns in Figure 10. This finding suggests that the temperature required for c-ZrO_2 formation is not maintained for a sufficient length of time during the cooling process, and hence the quantity of c-ZrO_2 formed is too low to be detected via XRD analysis.

Ramachandra Rao and Kannan [26] and Nagarajan and Rao [51] showed that the CaO released during the sintering of HA/ZrO_2 at temperatures of 1150 °C and above stabilizes the m-ZrO_2 via a solid solution reaction, and prompts the formation of t-ZrO_2. However, with the release of excess CaO through the further decomposition of FA, the solubility of Ca in ZrO_2 exceeds the maximum solid solution range and hence $CaZrO_3$ is formed in preference to t-ZrO_2 [52,53]. Heimann and Vu [52] showed that when CaO is added to HA/ZrO_2 composite sintered samples, the surplus CaO is effectively fixed by the ZrO_2, which acts as a sink for the Ca^{2+} ions. Consequently, either t-ZrO_2 or $CaZrO_3$ is formed. Furthermore, according to the ZrO_2-$CaZrO_3$ phase diagram [54], the formation of $CaZrO_3$ depends on the extent of CaO diffusion into ZrO_2. Hence, a fuller decomposition of FA promotes the production of $CaZrO_3$. However, in the present study, although the quantity of CaO increases significantly with an increasing laser power, that of t-ZrO_2 increases only slightly. Furthermore, the quantity of $CaZrO_3$ reduces under the highest laser power of 1200 W. By contrast, the quantity of $CaCO_3$ increases significantly with an increasing laser power. This feature suggests that given a sufficiently high laser energy, the tendency of CaO and CO_2 to react and form $CaCO_3$ is higher than that of CaO and ZrO_2 reacting to form $CaZrO_3$. However, further investigation is required to confirm this inference and to clarify the related underlying mechanisms.

3.4. Micro-Hardness Evaluation

Figure 11 shows the cross-sectional hardness profiles of the various specimens from the CL (thickness approximately 0.2–0.3 mm) through the TL and into the substrate. For all three samples, the TL has a higher hardness than the CL, which in turn has a greater hardness than the substrate. Comparing the CL hardness values of the three samples, it is seen that the hardness increases from 1100 $HV_{0.3}$ to 1300 $HV_{0.3}$ as the laser-cladding power is increased from 400 W to 800 W, but then reduces to around 800 $HV_{0.3}$ as the laser-cladding power is further increased to 1200 W. From inspection, the CL hardness of the three specimens is around 2~3 times higher than that of the Ti6Al4V substrate.

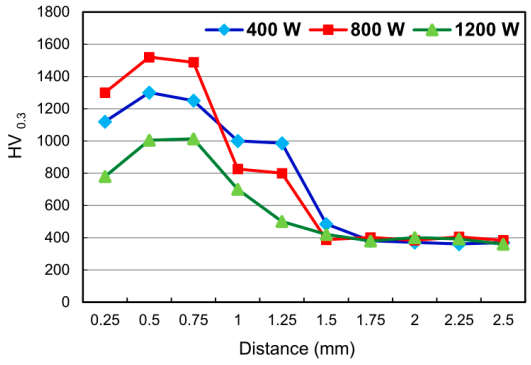

Figure 11. Cross-sectional hardness profiles of FA/ZrO_2 specimens prepared using different laser powers.

The hardness of laser-clad coatings is related to both their microstructural characteristics (e.g., porosity and density) and their phase constituents [41,43,55]. For the present samples, the CL microstructure exhibits a greater refinement and densification effect as the laser power (travel

speed) increases (see Figure 6). Consequently, the hardness increases. The phase constituents of the CL can be ranked in order of decreasing hardness as ZrO_2 > CaF_2 > CaO > $CaCO_3$ [56]. As shown in the XRD patterns in Figure 10, the sample prepared using a laser power of 1200 W has a high CaO and $CaCO_3$ (low hardness) content. Thus, the microstructure-induced hardness enhancement is outweighed by the softening effect of the CaO and $CaCO_3$ phases, and consequently a reduction in the CL hardness occurs.

Chien *et al.* [57] showed that the average hardness of the CL formed in the laser cladding of pure FA on Ti6Al4V substrates was equal to 617 $HV_{0.3}$ for a laser power of 740 W and 750 $HV_{0.3}$ for a laser power of 1150 W. It is noted that these hardness values are significantly lower than those obtained in the present study. The laser source and laser cladding parameters are similar in both cases. Hence, it is inferred that the higher CL hardness of the present specimens is due to the addition of ZrO_2 to the FA matrix. Kim *et al.* [41] prepared sintered FA samples containing 20 and 40 vol % ZrO_2 powder, respectively, and found that the hardness increased with an increasing ZrO_2 content. Ouyang *et al.* [43] used a laser-cladding process to deposit yttria partially stabilized ZrO_2 (7 wt %) ceramic coatings doped with 2.5 wt % TiO_2 on aluminum alloy substrates. The cladding layer was found to have a hardness of 1415~1575 $HV_{0.1}$. This value is greater than that observed for the present coatings. Kim *et al.* [41] conducted sintering trials using HA and FA powders doped with 20 vol % ZrO_2. The results showed that the FA-ZrO_2 composites had a greater hardness (~8 GPa) than the HA-ZrO_2 samples (~1 GPa). Various studies have attributed the greater hardness of laser-clad ZrO_2 or ZrO_2 composite coatings to the absence of porosity and a fine-grained structure [41,43]. However, the present results suggest that the hardness is actually determined by a competition process between the microstructural hardening effects and the phase composition softening effects.

4. Conclusions

The present study has deposited composite coatings consisting of fluorapatite (FA) and 20 wt % yttria (3 mol %) stabilized zirconia (ZrO_2, 3Y-TZP) on Ti6Al4V substrates using a laser cladding process with laser powers and travel speeds of 400 W/200 mm/min, 800 W/400 mm/min, and 1200 W/600 mm/min, respectively. The experimental findings support the following main conclusions.

1. The depth, width and depth/width ratio of the TL increase with an increasing laser power (travel speed). For the 800 W and 1200 W specimens, cracks are formed in the TL due to the greater cooling rate and larger weld zone (*i.e.*, greater shrinkage stress). However, no cracks are formed in the CL due to the addition of ZrO_2 to the FA powder and the relatively small CTE mismatch between the FA/ZrO_2 powders and the substrate.
2. A significant diffusion of alloying elements occurs between the CL and the TL. As a result, a good metallurgical bond is formed between them. Overall, the alloying elements of the TL are close to the composition of the substrate, while the alloying elements of the CL are close to the composition of the coating material.
3. The CL of the 400 W specimen consists mainly of FA, TTCP, CaF_2, $CaZrO_3$, $CaTiO_3$, m-ZrO_2 and a small amount of θ-Al_2O_3. For the 800 W specimen, the CL also contains CaO, $CaCO_3$ and trace amounts of t-ZrO_2. For the highest laser power of 1200 W, the CaO, $CaCO_3$ and TTCP contents of the CL increase significantly. The t-ZrO_2 content also increases. However, that of m-ZrO_2 and $CaZrO_3$ reduces. In general, the tendency to form composite phases increases as the laser power increases.
4. For all of the specimens, the TL has a greater hardness than the CL. Moreover, the CL hardness is around 2~3 times higher than that of the Ti6Al4V substrate. As the laser power increases from 400 W to 800 W, the CL hardness increases due to a microstructural refinement and densification effect. However, under the highest laser power of 1200 W, the hardness reduces significantly due to the formation of CaO and $CaCO_3$ phases with relatively low hardness.

Acknowledgments: The authors gratefully acknowledge the financial support provided to this research by the Chi Mei Foundation Hospital, China (Taiwan), under Grant Number 110990223 and the Ministry of Science and Technology of China (Taiwan) under Grant Number NSC 101-2221-E-218-017.

Author Contributions: Chi-Sheng Chien, Cheng-Wei Liu and Tsung-Yuan Kuo conceived and designed the experiments; Chi-Sheng Chien and Cheng-Wei Liu performed the experiments; Chi-Sheng Chien, Cheng-Wei Liu and Tsung-Yuan Kuo analyzed the data and discussed the experiment; Chi-Sheng Chien and Tsung-Yuan Kuo wrote the paper. The manuscript was reviewed by all authors.

Conflicts of Interest: The authors declare no conflict of interest.

References

1. Zhao, Y.T.; Zhang, Z.; Dai, Q.X.; Lin, D.Y.; Li, S.M. Microstructure and bond strength of HA(+ZrO_2 + Y_2O_3)/Ti6Al4V composite coatings fabricated by RF magnetron sputtering. *Surf. Coat. Technol.* **2006**, *200*, 5354–5363. [CrossRef]
2. Wang, B.C.; Chang, E.; Yang, C.Y.; Tu, D. A histomorphometric study on osteoconduction and osseointegration of titanium alloy with and without plasma-sprayed hydroxyapatite coating using back-scattered electron images. *J. Mater. Sci. Mater. Med.* **1993**, *4*, 394–403. [CrossRef]
3. Savarino, L.; Fini, M.; Ciapetti, G.; Cenni, E.; Granchi, D.; Baldini, N.; Greco, M.; Rizzi, G.; Giardino, R.; Giunti, A. Biologic effects of surface roughness and fluorhydroxyapatite coating on osteointegration in external fixation systems: An *in vivo* experimental study. *J. Biomed. Mater. Res. A* **2003**, *66*, 652–661. [CrossRef] [PubMed]
4. Khor, K.A.; Fu, L.; Lim, V.J.P.; Cheang, P. The effects of ZrO_2 on the phase compositions of plasma sprayed HA/YSZ composite coatings. *Mater. Sci. Eng. A* **2000**, *276*, 160–166. [CrossRef]
5. De Bruijn, J.D.; van Blitterswijk, C.A.; Davies, J.E. Initial bone matrix formation at the hydroxyapatite interface *in vivo*. *J. Biomed. Mater. Res.* **1995**, *29*, 89–99. [CrossRef] [PubMed]
6. Oonishi, H.; Iwaki, Y.; Kin, N.; Kushitani, S.; Murata, N.; Wakitani, S.; Imoto, K. Hydroxyapatite in revision of total hip replacements with massive acetabular defects. *J. Bone Jt. Surg.* **1997**, *79B*, 87–92. [CrossRef]
7. Sun, L.; Berndt, C.C.; Gross, K.A.; Kucuk, A. Material fundamentals and clinical performance of plasma-sprayed hydroxyapatite coatings: A review. *J. Biomed. Mater. Res.* **2001**, *58*, 570–592. [CrossRef] [PubMed]
8. Li, H.; Li, Z.X.; Li, H.; Wu, Y.Z.; Wei, Q. Characterization of plasma sprayed hydroxyapatite/ZrO_2 graded coating. *Mater. Des.* **2009**, *30*, 3920–3924. [CrossRef]
9. Wang, G.; Zreiqat, H. Review—Functional coatings or films for hard-tissue applications. *Materials* **2010**, *3*, 3994–4050. [CrossRef]
10. Chen, Y.; Miao, X. Thermal and chemical stability of fluorohydroxyapatite ceramics with different fluorine contents. *Biomaterials* **2005**, *26*, 1205–1210. [CrossRef] [PubMed]
11. Rawls, H.R.; Zimmerman, B.F. Fluoride-exchanging resins for caries for caries protection. *Caries Res.* **1983**, *17*, 32–43. [CrossRef] [PubMed]
12. Bhadang, K.A.; Gross, K.A. Influence of fluorapatite on the properties of thermally sprayed hydroxyapatite coatings. *Biomaterials* **2004**, *25*, 4935–4945. [CrossRef] [PubMed]
13. Weng, J.; Liu, X.; Zhang, X.; Ji, X. Thermal decomposition of hydroxyapatite structure induced by titanium and its dioxide. *J. Mater. Sci. Lett.* **1994**, *13*, 159–161. [CrossRef]
14. Moreno, E.C.; Kresak, M.; Zahradnik, R.T. Fluoridated hydroxyapatite solubility and caries formation. *Nature* **1974**, *247*, 64–65. [CrossRef] [PubMed]
15. Ingram, G.S.; Nash, P.F. Mechanism for the anticaries action of fluoride. *Caries Res.* **1980**, *14*, 298–303. [CrossRef] [PubMed]
16. Al-Noaman, A.; Karpukhina, N.; Rawlinson, S.C.F.; Hill, R.G. Effect of FA on bioactivity of bioactive glass coating for titanium dental implant. Part I: Composite powder. *J. Non-Cryst. Solids* **2013**, *364*, 92–98. [CrossRef]
17. Dhert, W.J.; Klein, C.P.; Jansen, J.A.; van der Velde, E.A.; Vriesde, R.C.; Rozing, P.M.; de Groot, K. A histological and histomorphometrical investigation of fluorapatite, magnesiumwhitlockite, and hydroxylapatite plasma-sprayed coatings in goats. *J. Biomed. Mater. Res.* **1993**, *27*, 127–138. [CrossRef] [PubMed]

18. Wei, M.; Evans, J.H.; Bostrom, T.; Grøndahl, L. Synthesis and characterization of hydroxyapatite, fluoride-substituted hydroxyapatite and fluorapatite. *J. Mater. Sci. Mater. Med.* **2003**, *14*, 311–320. [CrossRef] [PubMed]
19. Viswanath, B.; Ravishankar, N. Interfacial reactions in hydroxyapatite/alumina nanocomposites. *Scr. Mater.* **2006**, *55*, 863–866. [CrossRef]
20. Suchanek, W.; Yoshimura, M. Processing and properties of hydroxyapatite-based biomaterials for use as hard tissue replacement implants. *J. Mater. Res.* **1998**, *13*, 94–117. [CrossRef]
21. Gautier, S.; Champion, E.; Bernache-Assollant, D. Processing, microstructure and toughness of Al_2O_3 platelet-reinforced hydroxyapatite. *J. Eur. Ceram. Soc.* **1997**, *17*, 1361–1369. [CrossRef]
22. Li, J.; Fartash, B.; Hermansson, L. Hydroxyapatite-alumina composites and bone-bonding. *Biomaterials* **1995**, *16*, 417–422. [CrossRef]
23. Nasiri-Tabrizi, B.; Fahami, A. Synthesis and characterization of fluorapatite-zirconia composite nanopowders. *Ceram. Int.* **2013**, *39*, 4329–4337. [CrossRef]
24. Ben Ayed, F.; Bouaziz, J. Sintering of tricalcium phosphate-fluorapatite composites with zirconia. *J. Eur. Ceram. Soc.* **2008**, *28*, 1995–2002. [CrossRef]
25. Ramachandra Rao, R.; Kannan, T.S. Synthesis and sintering of hydroxyapatite-zirconia composites. *Mater. Sci. Eng. C* **2002**, *20*, 187–193. [CrossRef]
26. Sallemi, I.; Bouaziz, J.; Ben Ayed, F. Elaboration and characterization of bioceramic based on tricalcium phosphate and zirconia. *Int. J. Curr. Eng. Technol.* **2013**, *3*, 1691–1700.
27. Song, J.H.; Lee, J.H. Glycothermal synthesis and characterization of 3Y-TZP nanoparticles. *Korean J. Mater. Res.* **2009**, *19*, 412–416. [CrossRef]
28. Subbara, E.C. *Science and Technology of Zirconia*; Heuer, A.H., Hobbs, A.H., Eds.; The American Society: Columbus, OH, USA, 1981; Volume 3, pp. 1–24.
29. Chou, B.Y.; Chang, E.; Yao, S.Y.; Chen, J.M. Phase transformation during plasma spraying of hydroxyapatite—10-wt %-zirconia composite coating. *J. Am. Ceram. Soc.* **2002**, *85*, 661–669. [CrossRef]
30. Butler, E.P. Transformation-toughened zirconia ceramics. *Mater. Sci. Technol.* **1985**, *1*, 417–432. [CrossRef]
31. Nasiri-Tabrizi, B.; Fahami, A. Reaction mechanisms of synthesis and decomposition of fluorapatite-zirconia composite nanopowders. *Ceram. Int.* **2013**, *39*, 5125–5136. [CrossRef]
32. Piconi, C.; Maccauro, G. Review—Zirconia as a ceramic biomaterial. *Biomaterials* **1999**, *20*, 1–25. [CrossRef]
33. Tlotleng, M.; Akinlabi, E.; Shukla, M.; Pityana, S. Microstructures, hardness and bioactivity of hydroxyapatite coatings deposited by direct laser melting process. *Mater. Sci. Eng. C* **2014**, *43*, 189–198. [CrossRef] [PubMed]
34. Wang, D.G.; Chen, C.Z.; Ma, J.; Lei, T.Q. Microstructure of yttric calcium phosphate bioceramic coatings synthesized by laser cladding. *Appl. Surf. Sci.* **2007**, *253*, 4016–4020. [CrossRef]
35. Cheng, G.J.; Pirzada, D.; Cai, M.; Mohanty, P.; Bandyopadhyay, A. Bioceramic coating of hydroxyapatite on titanium substrate with Nd-YAG laser. *Mater. Sci. Eng. C* **2005**, *25*, 541–547. [CrossRef]
36. Chien, C.S.; Hong, T.F.; Han, T.J.; Kuo, T.Y.; Liao, T.Y. Effects of different binders on microstructure and phase composition of hydroxyapatite Nd-YAG laser clad coatings. *Appl. Surf. Sci.* **2011**, *257*, 2387–2393. [CrossRef]
37. Chien, C.S.; Liao, T.Y.; Hong, T.F.; Kuo, T.Y.; Chang, C.H.; Yeh, M.L.; Lee, T.M. Surface microstructure and bioactivity of hydroxyapatite and fluorapatite coatings deposited on Ti-6Al-4V substrates using Nd-YAG laser. *J. Med. Biol. Eng.* **2014**, *34*, 109–115. [CrossRef]
38. Chien, C.S.; Ke, Y.S.; Kuo, T.Y.; Liao, T.Y.; Lee, T.M.; Hong, T.F. Effect of TiO_2 addition on surface microstructure and bioactivity of fluorapatite coatings deposited using Nd:YAG laser. *Proc. Inst. Mech. Eng. H* **2014**, *228*, 379–387. [CrossRef] [PubMed]
39. Chien, C.S.; Ke, Y.S.; Kuo, T.Y.; Liao, T.Y.; Lin, H.C.; Lee, T.M. Surface properties and *in vitro* bioactivity of fluorapatite/TiO_2 coatings deposited on Ti substrates by Nd:YAG laser cladding. *J. Med. Biol. Eng.* **2015**, *35*, 357–366. [CrossRef]
40. Chien, C.S.; Liu, C.W.; Kuo, T.Y.; Wu, C.C.; Hong, T.F. Bioactivity of fluorapatite/alumina composite coatings deposited on Ti6Al4V substrates by laser cladding. *Appl. Phys. A* **2016**, *122*. [CrossRef]
41. Kim, H.W.; Kong, Y.M.; Koh, Y.H.; Kim, H.E.; Kim, H.M.; Ko, J.S. Pressureless sintering and mechanical and biological properties of fluor-hydroxyapatite composites with zirconia. *J. Am. Ceram. Soc.* **2003**, *86*, 2019–2026. [CrossRef]
42. Kelkar, G. *Pulsed Laser Welding*; WJM Technology: Cerritos, CA, USA. Available online: http://www.welding-consultant.com (accessed on 29 July 2011).

43. Ouyang, J.H.; Nowotny, S.; Richter, A.; Beyer, E. Laser cladding of yttria partially stabilized ZrO_2 (YPSZ) ceramic coatings on aluminum alloys. *Ceram. Int.* **2001**, *27*, 15–24. [CrossRef]
44. Song, W.; Zhu, P.; Cui, K. Effect of Ni content on cracking susceptibility and microstructure of laser-clad Fe-Cr-Ni-B-Si alloy. *Surf. Coat. Technol.* **1996**, *80*, 279–282.
45. Zhang, S.; Zeng, X.; Wang, Y.; Cheng, K.; Weng, W. Adhesion strength of sol-gel derived fluoridated hydroxyapatite coatings. *Surf. Coat. Technol.* **2006**, *200*, 6350–6354. [CrossRef]
46. Scardi, P.; Leoni, M.; Bertamini, L. Residual stresses in plasma sprayed partially stabilized zirconia TBCs: Influence of the deposition temperature. *Thin Solid Films* **1996**, *278*, 96–103. [CrossRef]
47. Zheng, X.B.; Ding, C.X. Characterization of plasma sprayed hydroxyapatite/TiO_2 composite coatings. *J. Therm. Spray Technol.* **2000**, *9*, 520–525. [CrossRef]
48. Ye, H.; Liu, X.Y.; Hong, H. Fabrication of titanium/fluorapatite composites and *in vitro* behavior in simulated body fluid. *J. Mater. Sci. Technol.* **2013**, *29*, 523–532. [CrossRef]
49. Ninga, C.Q.; Zhoub, Y. On the microstructure of biocomposites sintered from Ti, HA and bioactive glass. *Biomaterials* **2004**, *25*, 3379–3387. [CrossRef] [PubMed]
50. Ben Ayed, F.; Bouaziz, J.; Bouzouita, K. Calcination and sintering of fluorapatite under argon atmosphere. *J. Alloys Compd.* **2001**, *322*, 238–245. [CrossRef]
51. Nagarajan, V.S.; Rao, K.J. Structural, mechanical and biocompatibility studies of hydroxyapatite-derived composites toughened by zirconia addition. *J. Mater. Chem.* **1993**, *3*, 43–51. [CrossRef]
52. Heimann, R.B.; Vu, T.A. Effect of CaO on thermal decomposition during sintering of composite hydroxyapatite-zirconia mixtures for monolithic bioceramic implants. *J. Mater. Sci. Lett.* **1997**, *16*, 437–439. [CrossRef]
53. Wu, J.M.; Yeh, T.S. Sintering of hydroxyapatite-zirconia composite materials. *J. Mater. Sci.* **1988**, *23*, 3771–3777. [CrossRef]
54. Stubican, V.S.; Ray, S.P. Phase equilibria and ordering in the system ZrO_2-CaO. *J. Am. Ceram. Soc.* **1977**, *60*, 534–537. [CrossRef]
55. Li, J.; Chen, C. Effect of ZrO_2 (YPSZ) on microstructure characteristic and wear resistance of theTi_3Al/TiC laser-cladded ceramic layer on titanium alloy. *Int. J. Appl. Ceram. Technol.* **2012**, *9*, 947–952. [CrossRef]
56. Hardness of Minerals Va: Variation among Oxides and Oxysalts. Available online: http://www.gly.uga.edu/railsback/Fundamentals/HardnessTrends29VaL.pdf (accessed on 29 January 2008).
57. Chien, C.S.; Liao, T.Y.; Hong, T.F.; Kuo, T.Y.; Wu, J.L.; Lee, T.M. Investigation into microstructural properties of fluorapatite Nd-YAG laser clad coatings with PVA and WG binders. *Surf. Coat. Technol.* **2011**, *205*, 3141–3146. [CrossRef]